IEEE Access
Multidisciplinary | Rapid Review | Open Access Journal

Received 9 February 2026, accepted 28 February 2026, date of publication 4 March 2026, date of current version 13 March 2026.

Digital Object Identifier 10.1109/ACCESS.2026.3670417

RESEARCH ARTICLE

SCR Independent Polytopic Lyapunov Control for MMC HVDC Networks

ROHAN KAMAT TARCAR, (Graduate Student Member, IEEE), MARJAN POPOV, (Fellow, IEEE), AND ALEKSANDRA LEKIĆ, (Senior Member, IEEE)
Faculty of Electrical Engineering, Mathematics, and Computer Science, Delft University of Technology, 2628 CD Delft, The Netherlands
Corresponding author: Rohan Kamat Tarcar (R.KamatTarcar@tudelft.nl)

ABSTRACT The growing High-Voltage Direct Current transmission networks require modern control strategies in converter stations to ensure reliable operation and uninterrupted energy supply, particularly under unstable and low Short-Circuit ratio conditions. Conventional Grid Following converters become unstable in low Short-Circuit ratio scenarios, while modern Grid Forming converters, though more robust, exhibit slower dynamic response in high Short-Circuit ratio scenarios. This paper presents a hybrid control switching strategy based on polytopic Lyapunov functions that combines the strengths of Grid Following Control and Grid Forming Control strategies. Switching between these control strategies occurs at defined hyperplanes of polytopes derived from the state-space equations, enabling the system to maintain fast and stable performance under changing Short-Circuit ratio conditions of the grid. Because the method is grounded in polytopic Lyapunov function theory, it demonstrates inherent large-signal stability. This proposed Hybrid Control Strategy is validated using real-time $\acute{o}$ simulations, showing robust performance during Short-Circuit ratio variations, highlighting its potential for future High-Voltage Direct Current systems.

INDEX TERMS Grid following converter, grid forming converter, hybrid control strategy, modular multilevel converter, polytopic Lyapunov function.

I. INTRODUCTION

In recent years, High Voltage Direct Current (HVDC) transmission networks have become crucial for long-distance energy transmission [1]. Renewable energy sources are being increasingly connected to the grid using HVDC transmission networks using modular multilevel converter (MMC) stations. The overall Short-Circuit ratio of the grid (SCR) decreases due to the implementation of small-scale green energy measures at the distribution level and the decommissioning of coal power plants. Reduced SCR in the grid leads to voltage instability and reduces power delivery capabilities [2] in HVDC transmission grids. When this occurs, the conventional Grid Following Control (GFL) strategies implemented in the converter stations will fail [3]. The GFM control strategy performs effectively under low SCR conditions by providing voltage and frequency support; it responds slowly to stiff grid conditions (high SCR); Under strong grid conditions, the grid voltage and frequency dominate the system dynamics, thereby reducing the control authority of the GFM and weakening its power–angle interaction, leading to slower dynamic responses and potential control interaction, making the GFM less effective compared to GFL or the proposed **Hybrid Control Strategy (HCS)** under strong grid conditions. [4]. Therefore, a control algorithm that combines the merits of both converters is urgently needed. Existing methods often rely on small-signal assumptions, which limit their adaptability during fast transients or uncertain grid conditions. To address this, we propose a stability-guaranteed switching method based on polytopic Lyapunov functions (PLF) that accounts for dynamic behavior across a wide range of SCR conditions. Unlike threshold-based or frequency-derivative approaches, PLFs provide a mathematically rigorous way to define stability boundaries for multi-mode (multiple control strategies) systems, allowing switching decisions that are both

The associate editor coordinating the review of this manuscript and approving it for publication was Fabio Mottola.

robust to transient disturbances and valid for large operating changes [5].

A hybrid dynamical system consisting of a family of continuous-time subsystems and a rule governing the switch is called a switched system [6]. In this article, this term is renamed for clarity to highlight the application of this concept as an HCS. This research article explores an HCS that combines the advantages of GFL and GFM methods into a single approach. In [7], the authors use a switching sequence based on the rate of frequency change (RoCoF, $\frac{df}{dt}$) and frequency change (Δf) to detect disturbances and change the control strategies of GFM and GFL, and vice versa. However, this research is only carried out for small increments in step changes, or more specifically, for small signal changes. Whereas [8] uses the frequency change rate to adjust the MMC system's inertia-supporting power by changing the control parameters. In [9], the authors propose a novel switching approach that matches the reference of the inner current loops for the GFL and GFM strategies by using the grid power synchronization loop. However, it requires the steady-state operating points before and after the control strategy switch to be the same. In [10], the authors propose a unified control loop to smoothly transition between GFL mode and stand-alone (GFM) mode by defining the voltage and frequency ranges for each mode. In [11], the authors propose a flexible switching method to switch between two GFL control strategies (P-V and P-Q) based on the small signal stable operating zones. Reference [12] proposes a sliding mode control-based method for the MMC, which promises faster dynamics but uses the SCR parameter of the AC grid as an uncertainty. The authors of [13] propose a separate algorithm for the real-time estimation of grid impedance and, based on the estimates, change the GFM control strategy parameters to adapt to the change in the system SCR. In [14], the authors have implemented a Power Self-Synchronization Control loop for the GFL converter, which changes the setpoint of the active power depending on the SCR. The authors in [15] and [16] have implemented a switching control strategy based on the switching boundaries obtained from the open-loop transfer functions of grid impedance ratios, which are estimated using multiple complex coefficient filters (MCCF) combined with the recursive discrete Fourier transform (RDFT). Unlike existing strategies, the proposed HCS does not require steady-state matching, prior impedance estimation, or small-signal assumptions, and it can adapt its switching law in real time using stability surfaces derived from PLFs.

The HCS presented in this paper proposes switching criteria based on stability boundaries to adaptively optimize the operation of the converters in response to varying grid conditions. Using the principle of Polytopic Lyapunov functions (PLFs), the stability boundaries form hyperplanes in which entities such as i_d and i_q are surfaces, forming a polytope in 2-dimensional space. In the literature, it has been implemented to give the modulated signal to simple

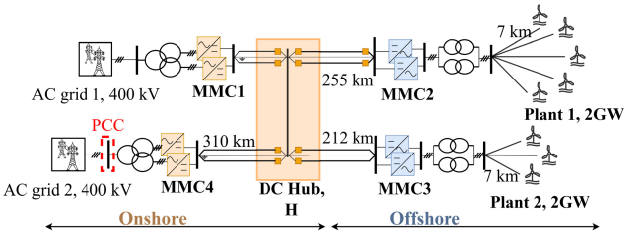

FIGURE 1. A four-terminal ±525 kV bipolar half-bridge MMC-based HVDC system with a metallic return and a DC Hub [19].

TABLE 1. Network specifications [19].

Parameter	Onshore	Offshore
Transformer capacity	5 GW	2.5 GW
Rated grid line-line voltage	400 kV	66 kV
Transformer voltage ratio	400/275 kV	275/66 kV
Transformer leakage reactance	0.18 pu	0.15 pu
Transformer configuration	Yn/Δ, 1P3W	Δ/Yn, 3P2W
DC line inductances	80 mH	80 mH
No. of MMC Submodules	240	240
Submodule capacitance	25 mF	16 mF
Converter Inductance	50 mH	50 mH

ĆUK and SEPIC DC-DC converters [17]. In this work, the algorithm has been improved to enable switching between GFL and energy-based GFM. Work done in [18] addresses switching safely during transient disturbances, whereas this work addresses which control mode guarantees stability under structural grid uncertainty (SCR change).

Section II covers the network model and the inner loop representation for MMC control. Sections III and IV discuss two control strategies implemented in the HCS. Section V presents the mathematical implementation of PLF-based control switching. Section VI examines the impact of AC-grid SCR on the selection of control strategies and the real-time results in the implementation of hybrid control. Section VII presents the conclusions.

II. NETWORK MODEL AND MMC INNER CONTROL LOOP

Fig. 1 shows a four-terminal ±525 kV bipolar half-bridge MMC-based HVDC system with a metallic return and a DC Hub. The network specifications are given in Table 1 as stated in [19]. The modeled network consists of two onshore stations and two offshore stations connected to Wind Power Parks (WPPs) connected radially to an onshore DC Hub as shown in Fig. 1. Furthermore, each station consists of two MMCs in a symmetrical bipolar configuration.

Fig. 2 depicts the MMC, which consists of three legs (one leg for every phase, i.e., $j \in \{a, b, c\}$) and two arms (upper and lower, denoted with U and L, respectively) in each leg. N_{SM} is the number of half-bridge submodules (SM) in every arm of the MMC. SMs are modeled using their averaged representations, with R_{arm} and L_{arm} being the equivalent resistance and inductance, respectively. Each SM has capacitance C_{SM}. The converter model is developed according to [20], using $\Sigma - \Delta$ nomenclature, all the variables

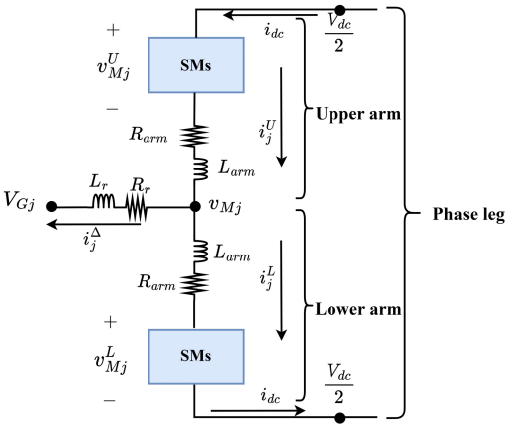

FIGURE 2. Diagram of one MMC leg, for $j \in \{a, b, c\}$.

in the converter can be represented as: $i_j^{\Delta} = i_j^U - i_j^L, i_j^{\Sigma} = \frac{i_j^U + i_j^L}{2}, v_{Mj}^{\Delta} = \frac{-v_{Mj}^U + v_{Mj}^L}{2}, v_{Mj}^{\Sigma} = \frac{v_{Mj}^U + v_{Mj}^L}{2}$.

By applying the Clarke-Park Transform to transform three-phase quantities (ABC) into a direct-quadrature (DQZ) frame [21], the set of differential equations is written in the dq-domain as:

$$\frac{d}{dt}\left(i_{dq}^{\Delta}\right) = \frac{v_{Mdq}^{\Delta} - \left(\omega L_{\text{eq}}^{\text{ac}} J_2 + R_{\text{eq}}^{\text{ac}} I_2\right) i_{dq}^{\Delta} - V_{Gdq}}{L_{\text{eq}}^{\text{ac}}}, \quad (1)$$

$$\frac{d}{dt}\left(V_{dq}^{\Delta}\right) = \omega J_2 V_{qd}^{\Delta} + \frac{N_{SM}}{C_{SM}} i_{dq}^{\Delta}, \quad (2)$$

where $L_{\text{eq}}^{\text{ac}} = L_r + \frac{L_{arm}}{2}$, $R_{\text{eq}}^{\text{ac}} = R_r + \frac{R_{arm}}{2}$, $J_2 = \begin{bmatrix} 0 & 1 \\ -1 & 0 \end{bmatrix}$, I_2 is an identity matrix with a size 2×2, and ω is the angular frequency. Furthermore, the vector $\Delta x(k) = \left[i_d^{\Delta}, i_q^{\Delta}\right]^T$ represents the state space variables and $\Delta u(k) = \left[v_{Md}^{\Delta} - V_{Gd}, v_{Mq}^{\Delta} - V_{Gq}\right]^T$ input variables. State-space matrices are:

$$A = \begin{bmatrix} -\frac{R_{\text{eq}}^{\text{ac}}}{L_{\text{eq}}^{\text{ac}}} & -\omega & 0 & 0 \\ \omega & -\frac{R_{\text{eq}}^{\text{ac}}}{L_{\text{eq}}^{\text{ac}}} & 0 & 0 \end{bmatrix}, \quad B = \text{diag}\left\{\frac{1}{L_{\text{eq}}^{\text{ac}}}, \frac{1}{L_{\text{eq}}^{\text{ac}}}\right\}, \quad (3)$$

which represents the inner control loop or cascaded current control loop of the MMC control strategies.

III. GFL CONTROL

The GFL-controlled converter can be seen as a current-controlled source with high parallel impedance. These converters require perfect synchronization with the AC grid frequency, achieved through a Phase-Locked Loop (PLL), to regulate the exchange of active and reactive power accurately. However, this synchronization process can lead to instability problems when the grid weakens, leading to fluctuations in the exchanged power and affecting the system's stability [22]. The internal dynamics of the PLL are not explicitly included in the state-space model to maintain analytical tractability of the hybrid control design. However, the PLL's estimated grid angle and frequency are incorporated as external signals within the GFL control framework, ensuring that its steady-state influence is retained. The potential impact of PLL bandwidth on the overall system stability will be analyzed in future work. The operation of the GFL converters is often regulated by a high-level controller (outer control loop), which sets the values of either P^*,[1] V_{dc}^*, Q^* and V_{rms}^*. The inner control loop controls and regulates the currents injected into the grid by determining the reference values $i_{d,q}^{*\Delta}$ [23], [24], [25]. In this article, the implemented control strategy is active power control for the d-axis and AC voltage control for the q-axis (outer loop), as shown in Fig. 3.

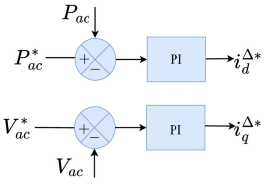

FIGURE 3. GFL control strategy.

The state space equations representing the GFL control strategies are shown as follows:

$$\dot{\xi}_{P_{\text{ac}}} = P_{\text{ac}}^* - P_{\text{ac}}, \quad i_d^{*\Delta} = K_P^{P_{\text{ac}}} \dot{\xi}_{P_{\text{ac}}} + K_I^{P_{\text{ac}}} \xi_{P_{ac}}, \quad (4)$$

$$\dot{\xi}_{V_{\text{ac}}} = V_{\text{ac}}^* - V_{\text{ac}}, \quad i_q^{*\Delta} = -K_P^{V_{\text{ac}}} \dot{\xi}_{V_{\text{ac}}} - K_I^{V_{\text{ac}}} \xi_{V_{\text{ac}}}, \quad (5)$$

$$\Delta x = \left[\xi_{P_{\text{ac}}}, \xi_{V_{\text{ac}}}\right]^T. \quad (6)$$

A combination of the inner and outer loop state space equations of the GFL control strategies yields to:

$$A = \begin{bmatrix} -\frac{R_{\text{eq}}^{\text{ac}}}{L_{\text{eq}}^{\text{ac}}} & -\omega_{GFL} & 0 & 0 \\ \omega_{GFL} & -\frac{R_{\text{eq}}^{\text{ac}}}{L_{\text{eq}}^{\text{ac}}} & 0 & 0 \\ 0 & 0 & K_I^{P_{\text{ac}}} & 0 \\ 0 & 0 & 0 & -K_I^{V_{\text{ac}}} \end{bmatrix}, \quad (7)$$

$$B = \text{diag}\left\{\frac{1}{L_{\text{eq}}^{\text{ac}}}, \frac{1}{L_{\text{eq}}^{\text{ac}}}, -K_P^{P_{\text{ac}}}, K_P^{V_{\text{ac}}}\right\}, \quad (8)$$

$$\Delta x(k) = \left[i_d^{\Delta}, i_q^{\Delta}, \xi_{P_{\text{ac}}}, \xi_{V_{\text{ac}}}\right]^T, \quad (9)$$

$$\Delta u(k) = \left[v_{Md}^{\Delta} - V_{Gd}, v_{Mq}^{\Delta} - V_{Gq}, \dot{\xi}_{P_{\text{ac}}}, \dot{\xi}_{V_{\text{ac}}}\right]^T. \quad (10)$$

This work uses the PLL output frequency ω_{PLL} in the GFL control equations. The internal dynamic states of the PLL are not explicitly included in the state-space model, as the primary focus is on the HCS. This simplification is valid under the assumption of a well-tuned PLL with bandwidth significantly higher than that of the outer control loops, such that its transient behavior has minimal influence on the stability boundaries derived using PLF. For low SCR conditions where PLL dynamics may strongly interact with converter control, the proposed HCS switches to GFM

[1] X^* denotes the reference value (setpoint) of X.

control. As the GFM control does not rely on a PLL, the adverse PLL dynamics are not present in the operating regime where they would have the most impact.

IV. GFM CONTROL

GFM controls behave as a voltage-controlled source with a low series impedance. They are mainly designed to set grid voltage and frequency at the Point of Common Coupling (PCC) and can operate in an islanded mode. Therefore, these voltage source converters need not be perfectly synchronized with the AC voltage of the grid. The operation of the GFM converters is often regulated by a voltage reference V^*_{AC} (outer loop) and frequency set points. This control strategy usually does not require inner current control when additional protection equipment is already used in the network. However, when inherent current limitation (over-current protection) is required, an inner control loop, similar to the one in the GFL control, can be added [23], [26], [27], which also improves the dynamic stiffness at the converter terminal. In this article, this inner loop is achieved by implementing a virtual capacitance, which decouples the voltage loop and facilitates the generation of $i^{*\Delta}_{d,q}$ references within this control framework [28]. Furthermore, implementing the concept of dual-port GFM (DP-GFM) control strategy, depicted in Figs. 4-6, which eliminates the need to assign distinct AC-GFM or DC-GFM roles to different converter stations, streamlining system dynamics and improving the resilience to topological changes or control reserve fluctuations [28]. During normal operation, DP-GFM maintains AC and DC voltages and power transfers within designated parameters and autonomously responds to load variations and contingencies, stabilizing the grid of grids. This approach enables energy exchange between the two ports without explicit mode switching or role designation. Therefore, the hybrid control strategy proposed in Section VI operates on top of this DP-GFM framework, and controls the switching between GFL and GFM behavior as a function of the grid SCR, while maintaining bidirectional power support across both ports. This is possible by adjusting the power injection autonomously to stabilize the MMC internal energy [28].

Using the phase angle generated as in Fig. 4, the state space equations representing the DP-GFM control equations for the outer loop depicted in Fig. 5 state space equations of the DP-GFM control strategy, and the inner loop state space equations are:

$$\dot{\xi}_{V_{Gd}} = V^*_{Gd} - V_{Gd}, \qquad \dot{\xi}_{V_{Gq}} = V^*_{Gq} - V_{Gq}, \tag{11a}$$

$$\xi_W = W^* - W, \qquad \dot{\xi}_W = -(P_{DC} - P_{\text{ac}}) \tag{11b}$$

$$\dot{\xi}_{V_{Gd}} = K_{Dp}(P^* - P) + V^*_{DC} - V_{DC} + K_{Dw}(-P_{DC} + P_{\text{ac}}) + K_{Pw}(W^* - W), \tag{11c}$$

$$V^*_{Gd} = K_I^{V_{Gd}} \xi_{V_{Gd}} + K_P^{V_{Gd}} \dot{\xi}_{V_{Gd}}, \tag{11d}$$

$$V^*_{Gq} = K_{rms}\left(V^*_{rms} - V_{rms}\right). \tag{11e}$$

From the inner control loop depicted in Fig. 6, the following equations can be derived:

$$i^{*\Delta}_d = K_P^{d\text{GFM}}\left(V^*_{Gd} - V_{Gd}\right) + K_I^{d\text{GFM}}\xi_{V_{Gd}} - \omega C_v\left(V^*_{Gq} - V_{Gq}\right) + \omega C_v V^*_{Gq}, \tag{12a}$$

$$i^{*\Delta}_q = K_P^{q\text{GFM}}\left(V^*_{Gq} - V_{Gq}\right) - K_I^{q\text{GFM}}\xi_{V_{Gq}} + \omega C_v\left(V^*_{Gd} - V_{Gd}\right) - \omega C_v V^*_{Gd}, \tag{12b}$$

$$\Delta x = \left[\xi_{V_{Gd}},\ \xi_{V_{Gq}}\right]^T, \tag{12c}$$

which combine the inner loop and outer loop state space equations of the GFM control strategies, so that we get new state space matrices:

$$A = \begin{bmatrix} -\frac{R^{\text{ac}}_{\text{eq}}}{L^{\text{ac}}_{\text{eq}}} & -\omega_{\text{GFM}} & 0 & 0 \\ \omega_{\text{GFM}} & -\frac{R^{\text{ac}}_{\text{eq}}}{L^{\text{ac}}_{\text{eq}}} & 0 & 0 \\ 0 & 0 & K_I^{d\text{GFM}} & 0 \\ 0 & 0 & 0 & -K_I^{q\text{GFM}} \end{bmatrix}, \tag{13}$$

$$B = \begin{bmatrix} \frac{1}{L^{\text{ac}}_{\text{eq}}} & 0 & 0 & 0 \\ 0 & \frac{1}{L^{\text{ac}}_{\text{eq}}} & 0 & 0 \\ 0 & 0 & -K_p^{d\text{GFM}} & -\omega C_v \\ 0 & 0 & \omega C_v & K_p^{q\text{GFM}} \end{bmatrix}, \tag{14}$$

$$G = \begin{bmatrix} 0 & 0 & 0 & 0 \\ 0 & 0 & 0 & 0 \\ 0 & 0 & 0 & \omega C_v \\ 0 & 0 & -\omega C_v & 0 \end{bmatrix}, \tag{15}$$

$$\Delta x(k) = \left[i^{\Delta}_d,\ i^{\Delta}_q, \xi_{V_{Gd}},\ \xi_{V_{Gq}}\right]^T, \tag{16}$$

$$\Delta u(k) = \begin{bmatrix} v^{\Delta}_{Md} - V_{Gd}, v^{\Delta}_{Mq} - V_{Gq}, \left(V^*_{Gd} - V_{Gd}\right), \\ \left(V^*_{Gq} - V_{Gq}\right) \end{bmatrix}^T. \tag{17}$$

the state $\Delta q(k) = \left[0, 0, V^*_{Gd}, V^*_{Gq}\right]^T$, is a constant, a set-point.

V. INFLUENCE OF SCR

The SCR of the equivalent grid connected to the MMC converter station at the PCC is modeled according to IEEE519-2014 [29]. IEEE519-2014 defines SCR as the ratio of short circuit current to that of load current at the PCC, which is further simplified below [30]:

$$X_g = \frac{1}{SCR}, \qquad L_g = \frac{X_g}{2\pi(f)}. \tag{18}$$

To show the theoretical link between the SCR and the change in steady-state operating points. Here is the theorem, with the accompanying proof.

Theorem 1: Under steady-state conditions and assuming a Thevenin equivalent model for the grid with impedance $Z_g = R_g + j\omega L_g$, the steady-state converter current components in the synchronous reference frame are

given by:

$$\overline{i_d^{\Delta}} = \frac{(R+R_g)(v_{Md}-V_{Gd}^{\text{ideal}}) + \omega(L_{\text{eq}}^{\text{ac}}+L_g)(v_{Mq}-V_{Gq}^{\text{ideal}})}{(R+R_g)^2+\omega^2(L_{\text{eq}}^{\text{ac}}+L_g)^2}$$

$$\overline{i_q^{\Delta}} = \frac{-\omega(L_{\text{eq}}^{\text{ac}}+L_g)(v_{Md}-V_{Gd}^{\text{ideal}}) + (R+R_g)(v_{Mq}-V_{Gq}^{\text{ideal}})}{(R+R_g)^2+\omega^2(L_{\text{eq}}^{\text{ac}}+L_g)^2}$$

and they are directly adjusted based on the grid impedance value.

Proof: Using and re-writing equation (1), we get:

$$v_{Md} = Ri_d^{\Delta} + L_{\text{eq}}^{\text{ac}}\frac{di_d^{\Delta}}{dt} - \omega L_{\text{eq}}^{\text{ac}} i_q^{\Delta} + V_{Gd}, \tag{19a}$$

$$v_{Mq} = Ri_q^{\Delta} + L_{\text{eq}}^{\text{ac}}\frac{di_q^{\Delta}}{dt} + \omega L_{\text{eq}}^{\text{ac}} i_d^{\Delta} + V_{Gq}. \tag{19b}$$

Assuming steady-state conditions (i.e., $\frac{di_d^{\Delta}}{dt} = \frac{di_q^{\Delta}}{dt} = 0$), the d-q axis equations become:

$$v_{Md} = R\,\overline{i_d^{\Delta}} - \omega L_{\text{eq}}^{\text{ac}}\,\overline{i_q^{\Delta}} + V_{Gd}, \tag{20a}$$

$$v_{Mq} = R\,\overline{i_q^{\Delta}} + \omega L_{\text{eq}}^{\text{ac}}\,\overline{i_d^{\Delta}} + V_{Gq}. \tag{20b}$$

The AC grid is modeled as a Thevenin equivalent with impedance $Z_g = R_g + j\omega L_g$. By incorporating the grid impedance, the effective voltages as experienced at the PCC are given by:

$$V_{Gd} = V_{Gd}^{\text{ideal}} - R_g\,\overline{i_d^{\Delta}} - \omega L_g\,\overline{i_q^{\Delta}}, \tag{21a}$$

$$V_{Gq} = V_{Gq}^{\text{ideal}} - R_g\,\overline{i_q^{\Delta}} + \omega L_g\,\overline{i_d^{\Delta}}. \tag{21b}$$

Substituting these into the original converter equations gives:

$$v_{Md} = (R+R_g)\,\overline{i_d^{\Delta}} - \omega(L_{\text{eq}}^{\text{ac}}+L_g)\,\overline{i_q^{\Delta}} + V_{Gd}^{\text{ideal}}, \tag{22a}$$

$$v_{Mq} = (R+R_g)\,\overline{i_q^{\Delta}} + \omega(L_{\text{eq}}^{\text{ac}}+L_g)\,\overline{i_d^{\Delta}} + V_{Gq}^{\text{ideal}}. \tag{22b}$$

By defining $A = R + R_g$, and $B = \omega(L_{\text{eq}}^{\text{ac}} + L_g)$, the the steady-state currents are:

$$\overline{i_d^{\Delta}} = \frac{A(v_{Md}-V_{Gd}^{\text{ideal}}) + B(v_{Mq}-V_{Gq}^{\text{ideal}})}{A^2+B^2}, \tag{23a}$$

$$\overline{i_q^{\Delta}} = \frac{-B(v_{Md}-V_{Gd}^{\text{ideal}}) + A(v_{Mq}-V_{Gq}^{\text{ideal}})}{A^2+B^2}. \tag{23b}$$

Substituting back the full expressions, we arrive at:

$$\overline{i_d^{\Delta}} = \frac{(R+R_g)(v_{Md}-V_{Gd}^{\text{ideal}}) + \omega(L_{\text{eq}}^{\text{ac}}+L_g)(v_{Mq}-V_{Gq}^{\text{ideal}})}{(R+R_g)^2+\omega^2(L_{\text{eq}}^{\text{ac}}+L_g)^2}, \tag{24a}$$

$$\overline{i_q^{\Delta}} = \frac{-\omega(L_{\text{eq}}^{\text{ac}}+L_g)(v_{Md}-V_{Gd}^{\text{ideal}}) + (R+R_g)(v_{Mq}-V_{Gq}^{\text{ideal}})}{(R+R_g)^2+\omega^2(L_{\text{eq}}^{\text{ac}}+L_g)^2}, \tag{24b}$$

which completes the proof. □

This theorem shows that the grid impedance is related to the steady-state values of the dq-component of the converter currents, i.e. $\overline{i_{d,q}^{\Delta}}$. As a consequence, by using PLF, we do not need the SCR estimator, as the dq-current errors are used in the states and not the states on their own. Therefore, the SCR change will influence the steady-state values directly without applying any calculation or estimation.

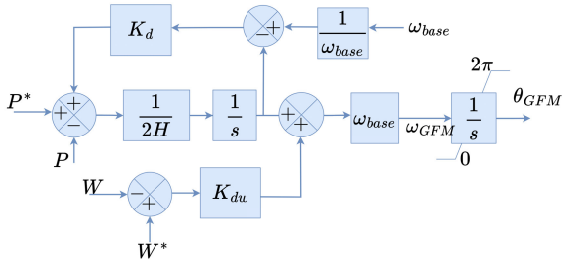

FIGURE 4. Phase angle generation for DP-GFM control.

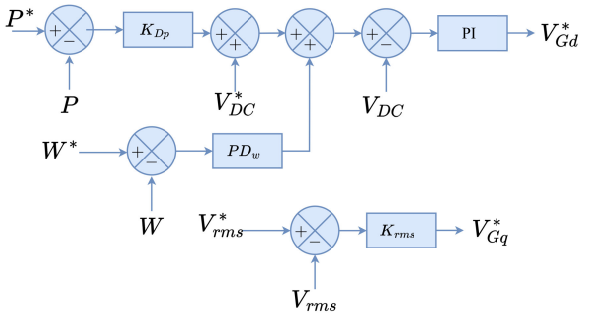

FIGURE 5. Outer control loop for DP-GFM control. Note: K_{Dp} denotes gain, while PD represents a proportional differential controller with K_{Pw} and K_{Dw} being proportional and differential gains, respectively.

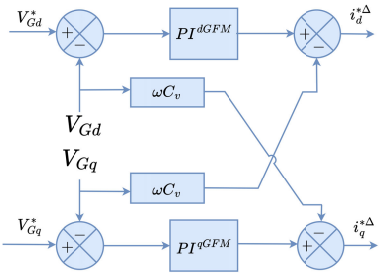

FIGURE 6. Modified DP-GFM control strategy with virtual capacitance.

VI. PLF-BASED HYBRID CONTROL METHODOLOGY

The PLF framework provides a unified stability analysis tool for systems represented as a convex combination of multiple linearized subsystems, wherein each subsystem corresponds to a specific operating mode (GFL and GFM) [18], [31]. A PLF ensures that the Lyapunov function remains positive definite for all vertices of the convex hull. This allows the stability of the overall hybrid system to be assessed even when switching occurs between control strategies [32]. The PLF-based switching framework divides the state space into multiple convex regions (in this case, two), each associated with a locally valid Lyapunov function. The switching law ensures that the system trajectory always evolves within

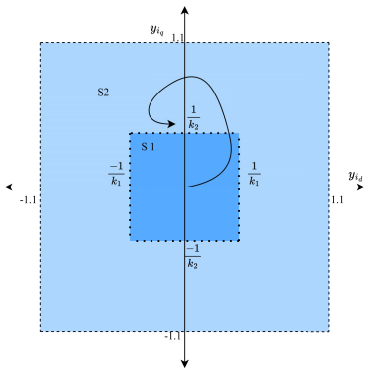

FIGURE 7. Polytope representation of the switching, where S1 and S2 represent the two states.

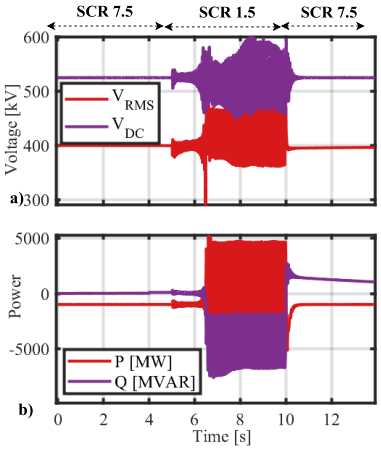

FIGURE 8. SCR change with GFL control described in Section III.

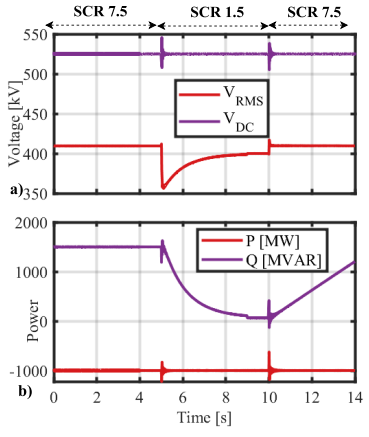

FIGURE 9. SCR change with DP-GFM control described in Section IV.

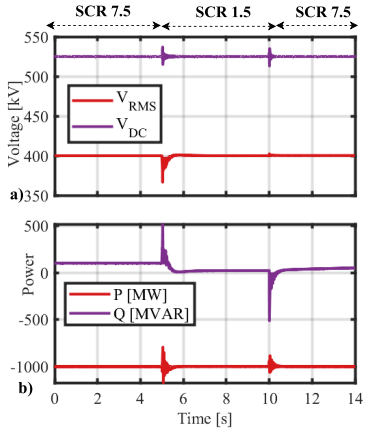

FIGURE 10. SCR change with HCS control described in Section V.

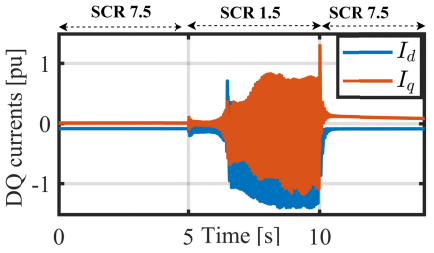

FIGURE 11. SCR change with GFL control described in Section III.

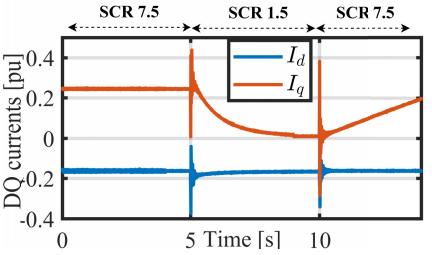

FIGURE 12. SCR change with DP-GFM control described in Section IV.

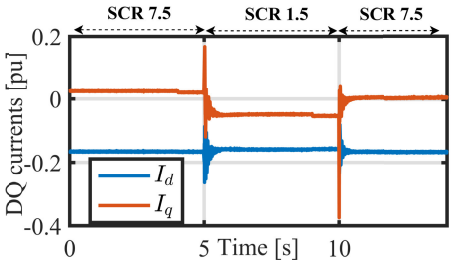

FIGURE 13. SCR change with HCS control described in Section V.

the union of stable subregions, thereby maintaining overall Lyapunov stability. As illustrated in Fig. 7, the system transitions from region $S1$ to $S2$ when the trajectory of the dq current errors crosses the boundary defined by the PLF hyperplanes. This transition represents a stability-driven control adaptation rather than a heuristic threshold-based switching. Here, it is considered that the steady-state values of the states of the state-space equations are denoted by $\bar{x}_{\text{GFL}}$ and $\bar{x}_{\text{GFM}}$. Thus, state variables for GFL in equation (9) control are as: $\bar{x}_{\text{GFL}} = \left[\bar{i}_d^{\Delta}, \bar{i}_q^{\Delta}, \bar{\xi}_{P_{\text{ac}}}, \bar{\xi}_{V_{\text{ac}}}\right]^T$. The values of $\dot{\bar{\xi}}_{P_{\text{ac}}}$ and $\dot{\bar{\xi}}_{V_{\text{ac}}}$ are equal to zero, as the steady-state value of the

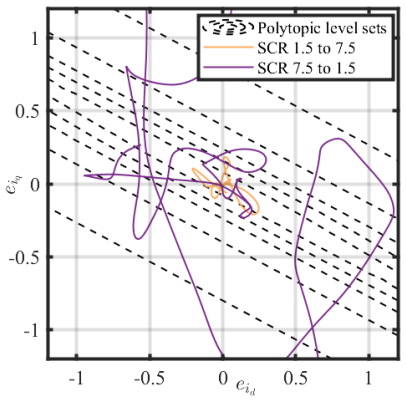

FIGURE 14. Phase portrait for GFL control for the SCR change shown in Fig. 8.

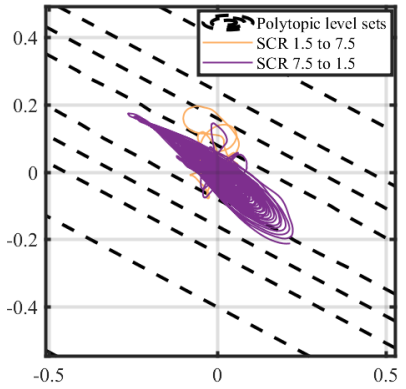

FIGURE 15. Phase portrait for DP-GFM control for the SCR change shown in Fig. 9.

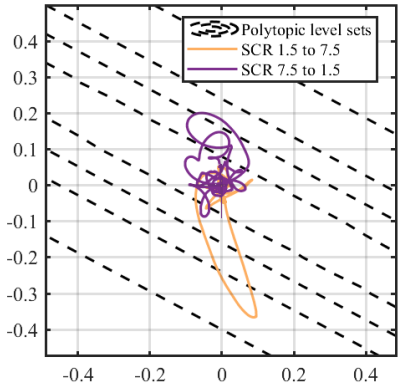

FIGURE 16. Phase portrait for HCS control for the SCR change shown in Fig. 10.

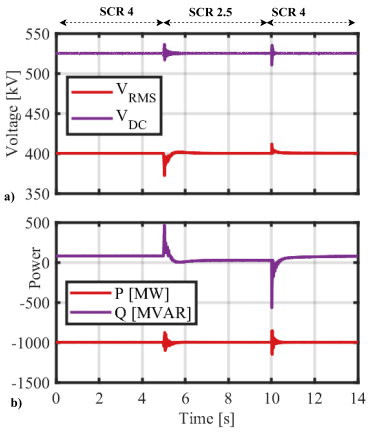

FIGURE 17. SCR change with GFL control described in Section III.

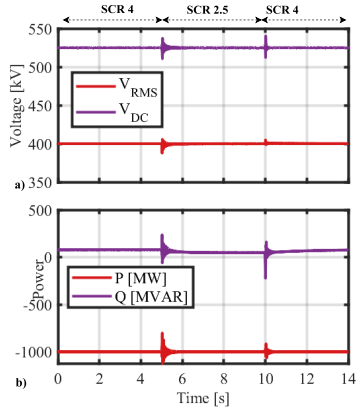

FIGURE 18. SCR change with DP-GFM control described in Section IV.

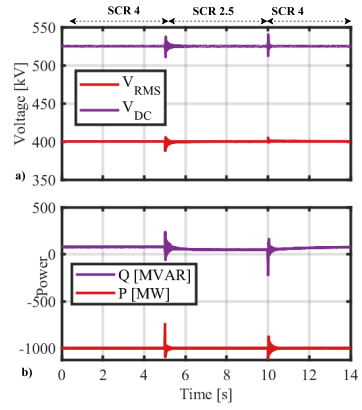

FIGURE 19. SCR change with HCS control described in Section V.

errors is 0. Therefore, the values of $\bar{\xi}_{P_{\text{ac}}}$ and $\bar{\xi}_{V_{\text{ac}}}$ are constants (C_i).

$$\bar{x}_{\text{GFL}} = \left[\bar{i}_d^{\Delta},\ \bar{i}_q^{\Delta},\ C_{P_{\text{ac}}},\ C_{V_{\text{ac}}}\right]^T. \tag{25}$$

Similarly, for GFM control state variables are $\bar{x}_{\text{GFM}} = \left[\bar{i}_d^{\Delta},\ \bar{i}_q^{\Delta},\ \bar{\xi}_{V_{Gd}},\ \bar{\xi}_{V_{Gq}}\right]^T$ and the values of $\dot{\bar{\xi}}_{V_{Gd}}$ and $\dot{\bar{\xi}}_{V_{Gq}}$ are equal to zero, since the steady-state value of the errors is 0. The values of $\bar{\xi}_{V_{Gd}}$ and $\bar{\xi}_{V_{Gq}}$ are constants (C_i). Furthermore,

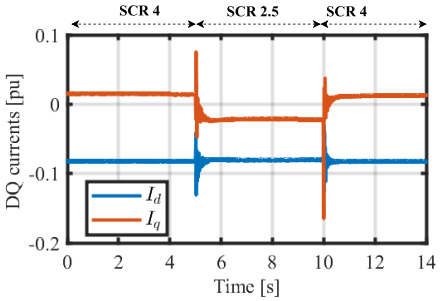

FIGURE 20. SCR change with GFL control described in Section III.

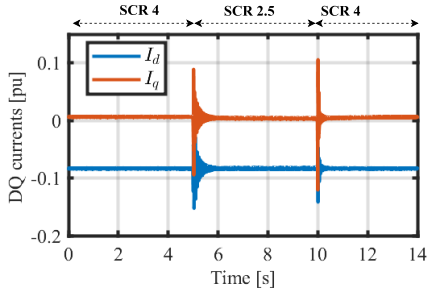

FIGURE 21. SCR change with DP-GFM control described in Section IV.

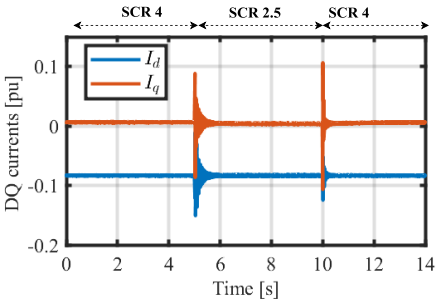

FIGURE 22. SCR change with HCS control described in Section V.

the steady-state values for GFM are:

$$\overline{x}_{\text{GFM}} = \left[\bar{i}_d^{\Delta},\ \bar{i}_q^{\Delta},\ C_{V_{Gd}},\ C_{V_{Gq}}\right]^T. \tag{26}$$

Now, let us define the system variables around its steady state as $y = x - \overline{x}$, which for the GFL and GFM controls are:

$$y_{\text{GFL}} = \begin{bmatrix} i_d^{\Delta} - \bar{i}_d^{\Delta} \\ i_q^{\Delta} - \bar{i}_q^{\Delta} \\ \xi_{P_{\text{ac}}} - C_{P_{\text{ac}}} \\ \xi_{V_{\text{ac}}} - C_{V_{\text{ac}}} \end{bmatrix}, \quad y_{\text{GFM}} = \begin{bmatrix} i_d^{\Delta} - \bar{i}_d^{\Delta} \\ i_q^{\Delta} - \bar{i}_q^{\Delta} \\ \xi_{V_{Gd}} - C_{V_{Gd}} \\ \xi_{V_{Gq}} - C_{V_{Gq}} \end{bmatrix}. \tag{27}$$

To be able to incorporate these changes in the system of ordinary differential equations describing the operation of GFM and GFL controls, the following change of variables is applied

$$\dot{y}_j = A_j(x - \overline{x}) + A_j\overline{x} + B_j = A_j y_j + \overline{B}_j, \tag{28}$$

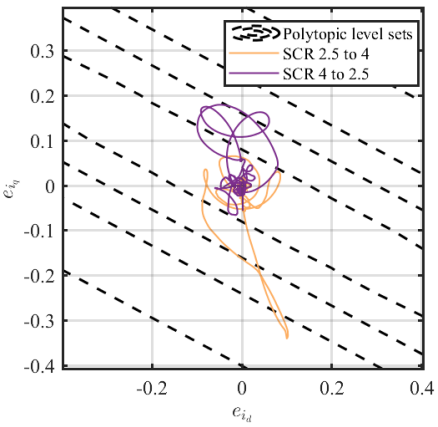

FIGURE 23. Phase portrait for GFL control for the SCR change shown in Fig. 17.

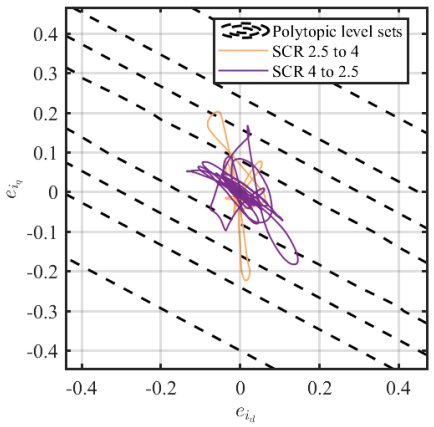

FIGURE 24. Phase portrait for DP-GFM control for the SCR change shown in Fig. 18.

where A_j, for $j \in \{\text{GFL}, \text{GFM}\}$, is the same as in (7) and (13), respectively, and, $\overline{B}_j = A_j\overline{x}_j + B_j$ is:

$$\overline{B}_{\text{GFL}} = \begin{bmatrix} -\frac{R_{\text{eq}}^{\text{ac}}}{L_{\text{eq}}^{\text{ac}}}\bar{i}_d^{\Delta} - \omega_{\text{GFL}}\bar{i}_q^{\Delta} + \frac{1}{L_{\text{eq}}^{\text{ac}}}\left(v_{Md}^{\Delta} - V_{Gd}\right) \\ -\frac{R_{\text{eq}}^{\text{ac}}}{L_{\text{eq}}^{\text{ac}}}\bar{i}_q^{\Delta} + \omega_{\text{GFL}}\bar{i}_d^{\Delta} + \frac{1}{L_{\text{eq}}^{\text{ac}}}\left(v_{Mq}^{\Delta} - V_{Gq}\right) \\ K_I^{P_{\text{ac}}} C_{P_{\text{ac}}} \\ -K_I^{V_{\text{ac}}} C_{V_{\text{ac}}} \end{bmatrix}, \tag{29}$$

and

$$\overline{B}_{\text{GFM}} = \begin{bmatrix} -\frac{R_{\text{eq}}^{\text{ac}}}{L_{\text{eq}}^{\text{ac}}}\bar{i}_d^{\Delta} - \omega_{\text{GFM}}\bar{i}_q^{\Delta} + \frac{1}{L_{\text{eq}}^{\text{ac}}}\left(v_{Md}^{\Delta} - V_{Gd}\right) \\ -\frac{R_{\text{eq}}^{\text{ac}}}{L_{\text{eq}}^{\text{ac}}}\bar{i}_q^{\Delta} + \omega_{\text{GFM}}\bar{i}_d^{\Delta} + \frac{1}{L_{\text{eq}}^{\text{ac}}}\left(v_{Mq}^{\Delta} - V_{Gq}\right) \\ K_I^{dGFM} C_{V_{Gd}} \\ -K_I^{q\text{GFM}} C_{V_{Gq}} \end{bmatrix}. \tag{30}$$

The polytopic Lyapunov function is defined using the infinity norm on the first two variables because, in this article, the effect of the other two states is not considered, and they do not contribute significantly to the behavior of the control

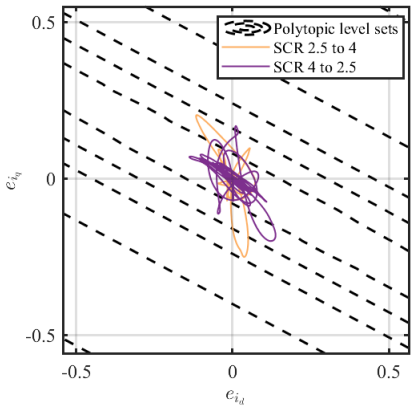

FIGURE 25. Phase portrait for HCS control for the SCR change shown in Fig. 19.

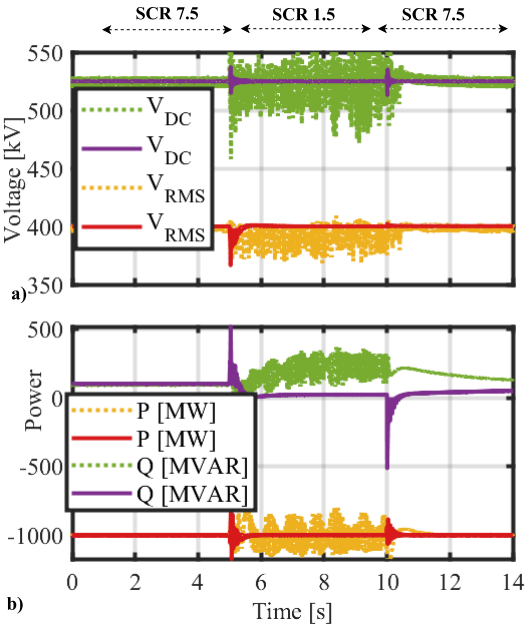

FIGURE 26. Comparison between Sliding mode control (dotted) and HCS (solid).

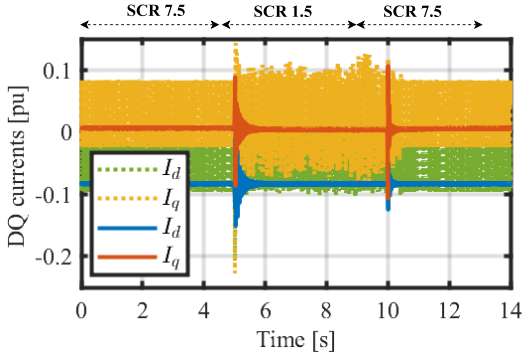

FIGURE 27. Comparison between Sliding mode control (dotted) and HCS (solid), dq currents.

strategies. Thus, the Lyapunov function is selected as:

$$V(y) = \max_{i\in\{1,2\}} |k_i y_i|\,, \quad y = [i_d^{\Delta}, i_q^{\Delta}]^T. \tag{31}$$

where $i \in I = \{GFL, GFM\}$. Then the polytope, as seen in Fig. 7, is defined as: Then the polytope is defined as:

$$\mathbf{P} = \left\{ y \in \mathbb{R}^2 : |k_i y_i| \le 1,\ i \in \{1,2\} \right\}. \tag{32}$$

Thus, the switching law governing the system is:

$$q = \begin{cases} 0 & \text{if } q = 1 \text{ and } k_i y_i \ge 1, \\ \{0,1\} & \text{if } q \in \{0,1\} \text{ and } -1 < k_i y_i < 1, \\ 1 & \text{if } q = 0 \text{ and } k_i y_i \le -1, \end{cases} \qquad i \in \{1,2\}. \tag{33}$$

Based on the previous derivation, we can define the following theorem.

Theorem 2: The overall HVDC system, which is switching between the GFL and GFM control modes, is globally bounded and asymptotically stable for a polytopic Lyapunov function defined in equation (31) that decreases along the system trajectories outside a defined polytope (32), if the values for coefficients $k_{\text{GFL-GFM},i} > 0$.

Proof: The proof is as follows.

Since the Lyapunov function is not differentiable everywhere (owing to the infinite norm and switching between controllers), we first show that the time derivative is negative where it exists and outside the polytope **P**. Filippov calculus can be applied at points of non-differentiability due to the intersection of controller switching, but for simplicity and insight, we first examine the classical time derivative.

Let $j = \arg\max_{i\in\{1,2\}} |k_i y_i|$ be the index of the active term in the Lyapunov function. Then, the Lyapunov derivative is:

$$\dot{V}(y) = k_j \dot{y}_j \operatorname{sgn}(k_j y_j),$$

where $\dot{y}_j$ is the j-th component of the GFL or GFM mode system dynamics. The sign function ensures the correct directionality of growth or decay. To guarantee the desired performance at the polytope facets, the coefficients k_i must satisfy the maximum allowed error values [17]. The reciprocal of these facets also acts as the stability margins of the control modes:

$$k_i = \pm|y_i| \text{ or } \frac{1}{k_i} = \pm\frac{1}{|y_i|} \tag{34}$$

Therefore, for GFL control, we have:

$$\frac{1}{k_{\text{GFL},1}} = \pm\frac{1}{|i_d^{\Delta} - \bar{i}_d^{\Delta}|}, \quad \frac{1}{k_{\text{GFL},2}} = \pm\frac{1}{|i_q^{\Delta} - \bar{i}_q^{\Delta}|}, \tag{35}$$

And for GFM:

$$\frac{1}{k_{\text{GFM},1}} = \pm\frac{1}{|i_d^{\Delta} - \bar{i}_d^{\Delta}|}, \quad \frac{1}{k_{\text{GFM},2}} = \pm\frac{1}{|i_q^{\Delta} - \bar{i}_q^{\Delta}|}. \tag{36}$$

Now, we analyze the system for four distinct cases: each control mode and dominant variable combination.

A. CASE 1: GFL MODE, $K_{GFL,1}$ ACTIVE (DOMINANT I_D^Δ)

$$\dot{V}_{\text{GFL}}(\mathbf{y}) = -k_{\text{GFL},1}\left(\mathbf{A}_{\text{GFL}}\langle 1, 1:4\rangle \mathbf{y} + \overline{\mathbf{B}}_{\text{GFL}}\langle 1\rangle\right)$$

$$\dot{V}(y) = -k_{\text{GFL},1}\left(-\frac{R_{\text{eq}}^{\text{ac}}}{L_{\text{eq}}^{\text{ac}}} i_d^\Delta - \omega_{\text{GFL}} i_q^\Delta + \frac{1}{L_{\text{eq}}^{\text{ac}}}(v_{Md}^\Delta - v_d^G)\right).$$

For $\dot{V}(y) < 0$, we require:

$$\frac{R_{\text{eq}}^{\text{ac}}}{L_{\text{eq}}^{\text{ac}}} i_d^\Delta + \omega_{\text{GFL}} i_q^\Delta < \frac{1}{L_{\text{eq}}^{\text{ac}}}(v_{Md}^\Delta - v_d^G),$$

Given that $v_{Md}^\Delta - v_d^G > 0$, the relation holds only when $k_{\text{GFL},1} > 0$.

B. CASE 2: GFM MODE, $K_{GFM,1}$ ACTIVE (DOMINANT I_D^Δ)

$$\dot{V}_{\text{GFM}}(\mathbf{y}) = k_{\text{GFM},1}\left(\mathbf{A}_{\text{GFM}}\langle 1, 1:4\rangle \mathbf{y} + \overline{\mathbf{B}}_{\text{GFM}}\langle 1\rangle\right)$$

$$\dot{V}(y) = k_{\text{GFM},1}\left(-\frac{R_{\text{eq}}^{\text{ac}}}{L_{\text{eq}}^{\text{ac}}} i_d^\Delta - \omega_{\text{GFM}} i_q^\Delta + \frac{1}{L_{\text{eq}}^{\text{ac}}}(v_{Md}^\Delta - v_d^G)\right),$$

leading to:

$$\frac{R_{\text{eq}}^{\text{ac}}}{L_{\text{eq}}^{\text{ac}}} i_d^\Delta + \omega_{\text{GFM}} i_q^\Delta > \frac{1}{L_{\text{eq}}^{\text{ac}}}(v_{Md}^\Delta - v_d^G),$$

Given that $v_{Md}^\Delta - v_d^G < 0$, the relation holds only when $k_{\text{GFM},1} > 0$.

C. CASE 3: GFL MODE, $K_{GFL,2}$ ACTIVE (DOMINANT I_Q^Δ)

$$\dot{V}_{\text{GFL}}(\mathbf{y}) = -k_{\text{GFL},2}\left(\mathbf{A}_{\text{GFL}}\langle 2, 1:4\rangle \mathbf{y} + \overline{\mathbf{B}}_{\text{GFL}}\langle 2\rangle\right)$$

$$\dot{V}(y) = -k_{\text{GFL},2}\left(-\frac{R_{\text{eq}}^{\text{ac}}}{L_{\text{eq}}^{\text{ac}}} i_q^\Delta - \omega_{\text{GFL}} i_d^\Delta + \frac{1}{L_{\text{eq}}^{\text{ac}}}(v_{Mq}^\Delta - v_q^G)\right),$$

Given that $v_{Md}^\Delta - v_d^G > 0$, the relation holds only when $k_{\text{GFL},2} > 0$.

D. CASE 4: GFM MODE, $K_{GFM,2}$ ACTIVE (DOMINANT I_Q^Δ)

$$v\dot{V}_{\text{GFM}}(\mathbf{y}) = k_{\text{GFM},2}\left(\mathbf{A}_{\text{GFM}}\langle 2, 1:4\rangle \mathbf{y} + \overline{\mathbf{B}}_{\text{GFM}}\langle 2\rangle\right)$$

$$\dot{V}(y) = k_{\text{GFM},2}\left(-\frac{R_{\text{eq}}^{\text{ac}}}{L_{\text{eq}}^{\text{ac}}} i_q^\Delta + \omega_{\text{GFM}} i_d^\Delta + \frac{1}{L_{\text{eq}}^{\text{ac}}}(v_{Mq}^\Delta - v_q^G)\right),$$

Given that $v_{Md}^\Delta - v_d^G < 0$, the relation holds only when $k_{\text{GFM},2} > 0$. □

For all the cases mentioned in Theorem 2, the argument is further solidified by substituting the numerical values from Table 2, leading to the expressions:

- Case 1: $0.02 i_d^\Delta + i_q^\Delta < 0.5246$,
- Case 2: $0.02 i_d^\Delta + i_q^\Delta > -1.307$,
- Case 3: $-0.02 i_q^\Delta + i_d^\Delta > -5.033$,
- Case 4: $-0.02 i_q^\Delta + i_d^\Delta < 1.652$.

By observing all polytope facets, we can conclude that conditions for coefficients are as stated in the theorem text, $k_{\text{GFL},1} = 6.667$, $k_{\text{GFL},2} = 12.5$, $k_{\text{GFM},1} = 5.882$, and $k_{\text{GFM},2} = 10$.

To conclude, in all cases, the time derivative $\dot{V}(y)$ is negative when the system is outside the polytope $\mathbf{P}$. The switching law ensures that switching occurs only when crossing the boundary of $\mathbf{P}$, thereby steering the system back inside. Inside $\mathbf{P}$, $V(y)$ remains bounded. Therefore, the overall hybrid system is globally bounded and asymptotically stable under the switching strategy.

One can note that the derivative of the PLF with respect to time is negative outside the region of the polytope $\mathbf{P}$. Checking the behavior of the system on the switching hyperplanes where the derivative of the PLF does not exist is crucial for the overall system stability, which can be carried out using the Filippov Criterion [33], [34]. By calculating all the possible facets of the polytope, $(\frac{1}{k})$ for the control strategies based on the values of MMCs given in Table 1, we obtain for GFL: $\frac{1}{k_{\text{GFL},1}} = 0.15$, $\frac{1}{k_{\text{GFL},2}} = 0.08$ and for GFM: $\frac{1}{k_{\text{GFM},1}} = 0.17$, $\frac{1}{k_{\text{GFM},2}} = 0.10$. The difference in the values of k_1 and k_2 is considered to be the buffer zones. It is worth noting that the proposed switching law is not a heuristic criterion but follows directly from the feasibility region of the polytopic Lyapunov function (PLF). Each controller (GFL or GFM) only admits a valid Lyapunov function within a specific SCR-dependent domain. When the operating point leaves this feasible region, the Lyapunov inequality is no longer satisfied, indicating that stability is uncertain. The hyperplanes, therefore, act as stability boundaries, ensuring that switching occurs only when required to preserve system stability. From a physical perspective, this corresponds to the transition between PLL-induced instability under weak SCR (favoring GFM) and adverse control-grid interaction under strong SCR (favoring GFL).

VII. RESULTS

The validation of the proposed HCS is carried out on the onshore converter MMC 4 of the HVDC system illustrated in Fig.1. MMC 4 is directly connected to the AC grid, making it the most relevant point for assessing the impact of the grid-strength variations on converter stability and control performance. The remaining converter terminals are maintained in steady-state operation to provide DC-link support and balanced system conditions. This approach isolates the influence of grid SCR variations on the local converter dynamics and provides a clear evaluation of the proposed control switching behavior. Table 2 summarizes the MMC setpoints and simulated values used for obtaining the results in a real-time environment in RSCAD. These parameters were selected following standard MMC tuning practices [18]. The proposed PLF-based switching framework inherently guarantees stability across the polytope of operating states, making the method less sensitive to small parameter perturbations.

Figs. 8, 9 and 10, show the behavior of the implemented control strategies when the SCR is changed from 7.5 (strong

TABLE 2. MMC setpoints and simulated values.

Quantity	Value	Quantity	Value
P^*	$1000MW$	V^*_{RMS}	$400kV$
$L^{\text{ac}}_{\text{eq}}$	$0.15pu$	$R^{\text{ac}}_{\text{eq}}$	$0.0034pu$
GFL, $\overline{V^M_d}$	$0.787pu$	GFL, $\overline{V^M_q}$	$0.787pu$
GFL, $\overline{V_d}$	$0.63pu$	GFL, $\overline{V_q}$	$0.032pu$
GFL, $\overline{i^*_d}$	$0.59pu$	GFL, $\overline{i^*_q}$	$0.06pu$
GFL, $\overline{i_d}$	$0.59pu$	GFL, $\overline{i_q}$	$0.06pu$
GFL,$K_I^{P_{\text{ac}}}$	$0.2s$	GFL,$K_I^{V_{\text{ac}}}$	$0.25s$
GFL,$K_P^{P_{\text{ac}}}$	$0.1pu$	GFL,$K_P^{V_{\text{ac}}}$	$0.09pu$
GFM, $\overline{V^M_d}$	$0.65pu$	GFM, $\overline{V^M_q}$	$0.6852pu$
GFM, $\overline{V_d}$	$0.454pu$	GFM, $\overline{V_q}$	$0.933pu$
GFM, $\overline{i^*_d}$	$-0.11pu$	GFM, $\overline{i^*_q}$	$-0.136pu$
GFM, $\overline{i_d}$	$-0.10pu$	GFM, $\overline{i_q}$	$-0.139pu$
GFM,$K_I^{d\text{GFM}}$	$0.46s$	GFM,$K_I^{q\text{GFM}}$	$0.49s$
GFM,$K_P^{d\text{GFM}}$	$0.21pu$	GFM,$K_P^{q\text{GFM}}$	$0.15pu$
GFM,K_{Dp}	$0.11pu$	GFM,$K_P^{W\text{GFM}}$	$0.13pu$
GFM,$K_D^{W\text{GFM}}$	$0.09s$	GFM,K_P^{DPd}	$0.15pu$
GFM,K_I^{DPd}	$0.21s$	GFM,K_{RMS}	$0.13pu$

grid) to 1.5 (weak grid), and then back to 7.5 (strong grid). Figs. 11, 12 and 13 show the behavior of the dq-current signals ($i_{d,q}$) for the said SCR change. Figs. 14, 15 and 16 show the phase portraits of the dq-current error signals ($e_{d,q} = i^{\Delta}_{d,q} - i^{*\Delta}_{d,q}$) for the same SCR change. Figs. 8a, 9a and 10a, show the V_{RMS} and V_{DC} converter voltages for when the SCR changes. Figs. 8b, 9b and 10b, portray the active (P) and reactive (Q) powers generated/absorbed by the MMC when the SCR changes occur. In Fig. 8, it can be seen that when the converter is connected to a strong grid, the GFL control strategy operates as expected, and the signals operate at their steady-state values. However, when the grid SCR is reduced, GFL is unable to maintain the steady-state values as the PLL is unable to function properly. This can be further explained by Fig. 14, which shows that when the SCR changes from 7.5 to 1.5, the error signals stray away from the origin and go towards the outer edges of the polytopic level sets where the control is borderline-unstable; it is then brought to below the levels sets (near the origin of the graph) when the SCR changes from 1.5 to 7.5. This is similarly evident from the time series plot of the dq-currents in Fig. 11. In Fig. 9, it can be seen that when the converter is connected to a strong grid, all the signals except the reactive power (in Fig. 9b) are at their expected operating set points. The reactive power is generated/absorbed by the converter to compensate for the lack of synchronization between the power angles of the AC grid and the angle generated by the GFM control strategy [35]. Fig. 15, shows that when the SCR changes to 1.5, the change in Q and V_{RMS}, causes the phase portrait of the current errors to move away from the origin but still well below the last level set, keeping the system in the stable zone. A similar trend can be seen from the time series plot of the dq-currents in Fig. 12. In Fig. 10, it can be seen that the HCS outperforms both GFL and GFM control strategies. The HCS seamlessly switches between the control strategies when the grid SCR changes to take advantage of GFL for strong grid conditions and GFM for weak grid conditions. Fig. 16, shows that the HCS has the most stable phase portrait of current errors as the trajectories are around the origin for both SCR changes and well inside the level sets, indicating that the system is stable. The time series plot of the dq-currents in Fig. 13 also illustrates this behavior.

Figs. 17, 18, and 19, show the behavior of the implemented control strategies when the SCR is changed from 4 (relatively stronger grid) to 2.5 (relatively weaker grid), and then back to 4. Figs. 20, 21 and 22 show the behavior of the dq-current signals ($i_{d,q}$) for the said SCR change. Figs. 23, 24, and 25 show the phase portraits of the dq-current error signals for the same SCR change. Figs. 17a, 18a and 19a, show the V_{RMS} and V_{DC} converter voltages for when the SCR changes. Figs. 17b, 18b and 19b, portray the active (P) and reactive (Q) powers generated/absorbed by the MMC when the SCR changes occur. In Fig. 17, it can be seen that when the converter is connected to a grid with SCR 4, the GFL control strategy operates as expected, and the signals operate at their steady-state values. When the grid SCR is reduced (to 2.5), GFL is still able to maintain the steady-state values of the electrical quantities, but the SCR change results in noticeable transients in V_{RMS} and Q as can be seen in Fig. 17. This can be further explained by Fig. 23, which shows that when the SCR changes from 4 to 2.5, the error signals stray away from the origin and go towards the farther polytopic level sets where the control is borderline-stable; it is then brought to below the levels sets (near the origin of the graph) when the SCR changes from 2.5 to 4. This is similarly evident from the time series plot of the dq-currents in Fig. 20. In Fig. 18, it can be seen that when the converter is connected to SCR 4, all the signals are at their expected operating set points. Fig. 24 shows that when the SCR changes to 2.5, there is a very slight dip in Q, causing the phase portrait of the current errors to move away from the origin but still well within the first level set for the most part, keeping the system in the stable zone. A similar trend can be seen from the time series plot of the dq-currents in Fig. 21. In Fig. 19, it can be seen that the HCS outperforms both GFL and GFM control strategies. The HCS seamlessly switches between the Control strategies when the grid SCR changes to take advantage of GFL for strong grid conditions and GFM for weak grid conditions, avoiding the sharp transients as seen in Fig. 17, and having relatively less sharp peaks than in Fig. 18. Fig. 25, shows that the HCS has a more relatively stable phase portrait of the current errors as the trajectories are around the origin for both SCR changes and well inside the level sets, indicating that the system is stable. The time series plot of the dq-currents in Fig. 22 also illustrates this behavior. To further validate our HCS against other controllers, we have implemented Sliding Mode Control (SMC) as modeled in [36]. Figs. 26 and 27 show the comparison between SMC and HCS when the SCR is changed from 7.5 (strong grid) to 1.5 (weak grid), and then back to 7.5 (strong grid). As shown in Fig. 26, the HCS outperforms the SMC in low SCR scenarios. Fig. 27, shows that the dq currents under Sliding Mode Control (SMC) exhibit persistent oscillations. Although the magnitude of the tracking error remains small, these oscillations are tolerated

by the system, indicating a borderline stable behavior. This persistent oscillatory response highlights one of the inherent drawbacks of SMC, namely the presence of chattering and sustained switching activity even near the desired operating point.

VIII. CONCLUSION

This research presents a hybrid control strategy that enables seamless transitions between GFL and GFM control modes to enhance the system performance through state hyperplanes. The proposed HCS is inherently a large signal stable, based on PLFs, allowing seamless transitions between the control strategies in response to changes in grid SCR. This research harnesses the merits of both GFL and GFM control strategies and demonstrates the robustness of the proposed methodology. By combining two control strategies with a switching rule, the HCS forms a nonlinear control system that is more responsive than conventional linear approaches. This HCS achieves the intended control objectives and enhances system resiliency and flexibility. Its effectiveness is validated through real-time simulations in RSCAD, demonstrating its practical relevance in HVDC for scenarios requiring high adaptability and dynamic performance. Future work will focus on extending this study through a detailed quantitative benchmarking of the proposed HCS against established control methods, such as sliding-mode and self-synchronization strategies, to further substantiate its practical and dynamic advantages. A comprehensive robustness analysis under parameter and measurement variations, as well as across a wider range of operating conditions (including SCR variations and transient disturbances), will also be carried out. In addition, explicit PLL dynamic modeling will be incorporated to further enhance the accuracy and generality of the stability assessment.

REFERENCES

[1] Z. Li, R. Zhan, Y. Li, Y. He, J. Hou, X. Zhao, and X.-P. Zhang, "Recent developments in HVDC transmission systems to support renewable energy integration," *Global Energy Interconnection*, vol. 1, no. 5, pp. 595–607, 2018.

[2] T. Joseph, C. U. Loo, G. Li, J. Liang, O. D. Adeuyi, M. H. Rahman, and I. Cowan, "Impact of grid strength on HVDC connection requirements," in *Proc. IEEE 12th Energy Convers. Congr. Exposit. - Asia (ECCE-Asia)*, May 2021, pp. 586–591.

[3] S. Peyghami, H. Mokhtari, F. Blaabjerg, and Y. Yang, "Grid synchronization for distributed generations," in *Encyclopedia of Sustainable Technologies*. Amsterdam, The Netherlands: Elsevier, 2023, pp. 1–21.

[4] H. Wu and X. Wang, "Control of grid-forming VSCs: A perspective of adaptive fast/slow internal voltage source," *IEEE Trans. Power Electron.*, vol. 38, no. 8, pp. 10151–10169, Aug. 2023. [Online]. Available: https://api.semanticscholar.org/CorpusId:254274999

[5] T. L. Vu and K. Turitsyn, "Lyapunov functions family approach to transient stability assessment," *IEEE Trans. Power Syst.*, vol. 31, no. 2, pp. 1269–1277, Mar. 2016.

[6] D. Liberzon and A. S. Morse, "Basic problems in stability and design of switched systems," *IEEE Control Syst.*, vol. 19, no. 5, pp. 59–70, 1999.

[7] W. Qiu, Q. Yang, T. Yang, X. Ma, X. Xiao, H. Shi, Y. Zhao, and S. Liang, "A grid forming/following sequence switching control strategy for supporting frequency stability of isolated power grids," in *Proc. 5th Asia Energy Electr. Eng. Symp. (AEEES)*, Mar. 2023, pp. 212–217.

[8] X. Lv, J. Wang, Z. Zhang, Z. Liu, and Z. Li, "Adaptive active inertia control strategy of MMC-HVDC systems for flexible frequency support," *Electronics*, vol. 12, no. 20, p. 4288, Oct. 2023. [Online]. Available: https://www.mdpi.com/2079-9292/12/20/4288

[9] X. Gao, D. Zhou, A. Anvari-Moghaddam, and F. Blaabjerg, "Seamless transitions between grid-following and grid-forming control: A novel switching method," in *Proc. 11th Int. Conf. Power Electron. ECCE Asia (ICPE ECCE Asia)*, May 2023, pp. 1154–1160.

[10] M. Kwon, S. Park, C.-Y. Oh, J. Lee, and S. Choi, "Unified control scheme of grid-connected inverters for autonomous and smooth transfer to stand-alone mode," *IEEE Trans. Power Electron.*, vol. 37, no. 1, pp. 416–425, Jan. 2022.

[11] M. Peng, L. Feng, X. Hao, M. Sun, W. Jiang, and C. Guo, "Flexible switching method of control strategy for MMC-HVDC converter based on AC power grid strength," *Frontiers Electron.*, vol. 5, Jan. 2025. [Online]. Available: https://www.frontiersin.org/journals/electronics/articles/10.3389/felec.2024.1475338

[12] F. Gharaghani and M. Asadi, "Robust sliding mode control for the MMC-HVDC transmission system with SCR uncertainty," *IET Power Electron.*, vol. 17, no. 15, pp. 2549–2560, Nov. 2024.

[13] S. Zhao and S.-K. Sul, "Real-time grid parameter estimation with grid-forming converters for robust synchronous power control," *J. Power Electron.*, vol. 24, no. 1, pp. 159–170, Jan. 2024.

[14] P. Wang, J. Ma, R. Zhang, S. Wang, T. Liu, Z. Wu, and R. Wang, "Power self-synchronization control of grid-forming voltage-source converters against a wide range of short-circuit ratio," *IEEE Trans. Power Electron.*, vol. 38, no. 12, pp. 15419–15432, Dec. 2023.

[15] M. Li, X. Zhang, Z. Guo, J. Wang, and F. Li, "The dual-mode combined control strategy for centralized photovoltaic grid-connected inverters based on double-split transformers," *IEEE Trans. Ind. Electron.*, vol. 68, no. 12, pp. 12322–12330, Dec. 2021.

[16] M. Li, X. Zhang, Z. Guo, H. Pan, M. Ma, and W. Zhao, "Impedance adaptive dual-mode control of grid-connected inverters with large fluctuation of SCR and its stability analysis based on D-partition method," *IEEE Trans. Power Electron.*, vol. 36, no. 12, pp. 14420–14435, Dec. 2021.

[17] A. Lekic, D. Stipanovic, and N. Petrovic, "Controlling the cuk converter using polytopic Lyapunov functions," *IEEE Trans. Circuits Syst. II, Exp. Briefs*, vol. 65, no. 11, pp. 1678–1682, Nov. 2018.

[18] R. K. Tarcar, M. Popov, and A. Lekić, "Polytopic Lyapunov function-based hybrid switching control strategy for high voltage direct current networks," *IEEE Open Access J. Power Energy*, vol. 12, pp. 442–454, 2025.

[19] R. K. Tarcar, A. Shetgaonkar, M. Popov, M. van der Meijden, W. Winter, M. Ndreko, R. Dimitrovski, M. Burkhardt, and A. Lekić, "Post DC fault circulating current suppression control," in *Proc. IEEE Power Energy Soc. Gen. Meeting (PESGM)*, Jul. 2023, pp. 1–5.

[20] Ö. C. Sakinci, A. Lekić, and J. Beerten, "Generalized impedance-based AC/DC power system modeling for harmonic stability analysis," *Int. J. Electr. Power Energy Syst.*, vol. 143, Jul. 2022, Art. no. 108456.

[21] G. Bergna-Diaz, J. Freytes, X. Guillaud, S. D'Arco, and J. A. Suul, "Generalized voltage-based state-space modeling of modular multilevel converters with constant equilibrium in steady state," *IEEE J. Emerg. Sel. Topics Power Electron.*, vol. 6, no. 2, pp. 707–725, Jun. 2018.

[22] N. Mohammed, W. Zhou, and B. Bahrani, "Comparison of PLL-based and PLL-less control strategies for grid-following inverters considering time and frequency domain analysis," *IEEE Access*, vol. 10, pp. 80518–80538, 2022.

[23] J. Rocabert, A. Luna, F. Blaabjerg, and P. Rodríguez, "Control of power converters in AC microgrids," *IEEE Trans. Power Electron.*, vol. 27, no. 11, pp. 4734–4749, Nov. 2012.

[24] K. V. Kkuni and G. Yang, "Effects of current limit for grid forming converters on transient stability: Analysis and solution," *Int. J. Electr. Power Energy Syst.*, vol. 158, Jul. 2024, Art. no. 109919.

[25] M. A. Desai, X. He, L. Huang, and F. Dörfler, "Saturation-informed current-limiting control for grid-forming converters," *Electric Power Syst. Res.*, vol. 234, Sep. 2024, Art. no. 110746.

[26] A. W. D. S. Serra, L. A. D. S. Ribeiro, and M. Savaghebi, "Disturbance decoupling in grid-forming inverters for enhanced dynamic response," *Eletrônica de Potência*, vol. 30, Mar. 2025, Art. no. e202528.

[27] A. W. D. S. Serra, L. A. D. S. Ribeiro, and M. Savaghebi, "A multi-loop control for grid-forming converters with enhanced dynamics," in *Proc. Energy Convers. Congr. Expo Eur. (ECCE Europe)*, Sep. 2024, pp. 1–7.

[28] X. Lyu, I. Subotić, and D. Groß, "Unified grid-forming control of PMSG wind turbines for fast frequency response and MPPT," 2022, *arXiv:2207.09536*.
[29] D. C. of the IEEE Power and E. Society, "Ieee recommended practice and requirements for harmonic control in electric power systems sponsored by the transmission and distribution committee ieee power and energy society," 2014.
[30] E. Rokrok, T. Qoria, A. Bruyere, B. Francois, and X. Guillaud, "Effect of using pll-based grid-forming control on active power dynamics under various scr,".
[31] C. Böhm, M. Lazar, and F. Allgöwer, "A relaxation of Lyapunov conditions and controller synthesis for discrete-time periodic systems," in *Proc. 49th IEEE Conf. Decis. Control (CDC)*, Dec. 2010, pp. 3277–3282.
[32] F. Zobiri, N. Meslem, and B. Bidegaray-Fesquet, "Event-triggered stabilizing controllers for switched linear systems," *Nonlinear Anal., Hybrid Syst.*, vol. 36, May 2020, Art. no. 100831.
[33] Y. Ohta, "On the construction of piecewise linear Lyapunov functions," in *Proc. 40th IEEE Conf. Decis. Control*, vol. 3, 2001, pp. 2173–2178.
[34] A. F. Filippov, "Differential equations with discontinuous right-hand side," *Matematicheskii Sbornik*, vol. 93, no. 1, pp. 99–128, 1960.
[35] S. Peyghami, H. Mokhtari, F. Blaabjerg, and Y. Yang, "Grid synchronization for distributed generations," in *Encyclopedia of Sustainable Technologies: Reference Module in Earth Systems and Environmental Sciences*. Amsterdam, The Netherlands: Elsevier, 2017, pp. 179–194.
[36] M. Aghahadi, L. Piegari, A. Lekic, and A. Shetgaonkar, "Sliding mode control of the MMC-based power system," in *Proc. 48th Annu. Conf. IEEE Ind. Electron. Soc.*, Oct. 2022, pp. 1–6.

ROHAN KAMAT TARCAR (Graduate Student Member, IEEE) received the M.Sc. degree in electrical power engineering from Delft University of Technology (TU Delft), The Netherlands, in 2023, where he is currently pursuing the Ph.D. degree. His research interests include real-time transient stability analysis, advanced HVDC control strategies, hybrid control schemes, Lyapunov-based stability methods, and the design and operation of multi-terminal HVDC (MTDC) networks for future power systems.

MARJAN POPOV (Fellow, IEEE) received the Ph.D. degree in electrical power engineering from Delft University of Technology, Delft, The Netherlands, in 2002. He is also a Chevening Alumnus. In 1997, he was an Academic Visitor with the University of Liverpool, Liverpool, U.K., working in the Arc Research Group on modeling SF6 circuit breakers. His main research interests include large-scale power system transients, intelligent protection for future power systems, and wide-area monitoring and protection. He is a member of Cigre and actively participated in WG C4.502 and WG A2/C4.39. In 2010, he received the prestigious Dutch Hidde Nijland Prize for extraordinary research achievements. He was a recipient of the IEEE PES Paper Award and the IEEE Switchgear Committee Award, in 2011. He was an Associate Editor of *International Journal of Electrical Power and Energy Systems* (Elsevier). He is a Senior Editor of *Advances in Electrical Engineering, Electronics, and Energy* (e-Prime).

ALEKSANDRA LEKIĆ (Senior Member, IEEE) received the B.S., M.S., and Ph.D. degrees in electrical engineering from the School of Electrical Engineering, University of Belgrade, Belgrade, Serbia, in 2012, 2013, and 2017, respectively. She is currently with the Faculty of Electrical Engineering, Mathematics, and Computer Science, TU Delft. She was an Assistant Professor, from January 2020 to April 2025. She has been an Associate Professor, since May 2025. She leads the Control of the HVDC/ac power systems team, which conducts advanced research in the field of power electronics and power system control. She was a recipient of the prestigious NWO Veni 2022 grant in The Netherlands. She is an Associate Editor of *International Journal of Electrical Power and Energy Systems* (Elsevier).